Ductile fracture simulation of cold-formed high strength steel using GTN damage model

Yan, Rui; Xin, Haohui; Veljkovic, Milan

DOI
10.1016/j.jcsr.2021.106832

Publication date
2021

Document Version
Final published version

Published in
Journal of Constructional Steel Research

Journal of Constructional Steel Research 184 (2021) 106832

Contents lists available at ScienceDirect

Journal of Constructional Steel Research

Ductile fracture simulation of cold-formed high strength steel using GTN damage model

Rui Yan [a], Haohui Xin [b,*], Milan Veljkovic [a]

[a] Faculty of Civil Engineering and Geosciences, Delft University of Technology, the Netherlands
[b] Department of Civil Engineering, School of Human Settlements and Civil Engineering, Xi'an Jiaotong University, China

ARTICLE INFO

Article history:
Received 19 March 2021
Received in revised form 21 June 2021
Accepted 25 June 2021
Available online 30 June 2021

Keywords:
High strength steel
Gurson-Tvergaard-Needleman (GTN) damage model
Stress triaxiality
Two-scale homogenisation

ABSTRACT

The use of high strength steel (HSS) cold-formed hollow section is of significant interest in the construction sector due to competitive costs. The accurate simulation of ductile fracture failure at the micro and macro scale is critical for improving the validity of predicting structural behaviour of HSS cold-formed hollow sections and welded joints. In this study, the ductile failure of the cold-formed S700 material is studied using the Gurson-Tvergaard-Needleman (GTN) damage model. Representative volume element (RVE) models with the void volume fraction (VVF) between 0.1% and 30% are employed to investigate the pressure dependency of the deviatoric limit stress. Different load conditions corresponding to different stress triaxiality levels are applied to unit cells with random spherical pores. The inelastic response of the unit cells are analysed, and the parameters q_1, q_2, and q_3 in the GTN yield surface are calibrated. An equation is proposed to determine parameter q_1 for different VVFs. The parameters critical VVF f_c and final VVF f_f are calibrated by the coupon test from the literature. Finally, the calibrated GTN model is validated against notched coupon tests. The finite element (FE) results show good agreement with the experimental results, indicating that the identified GTN model could efficiently predict the behaviour of the cold-formed HSS.

1. Introduction

The existing rules for the design of steel structures according to Eurocodes are limited to the material behaviour of mild steels with the steel grade up to S460. Supplementary rules proposed in EN1993-1-12 [1] are used to design structures made of cold-formed high strength steel (HSS) hollow sections. These supplementary rules will be integrated into revised versions of EN1993 design standard parts, and only "Additional rules for steel grades up to S960" will remain in a new version of EN1993-1-12. A welded HSS joint, comprised of the base material, the weld metal, and the heat affected zone (HAZ), has less ductility than a welded mild steel joint. It is an open question whether the research on hollow section joints undertaking worldwide is sufficiently systematic and comprehensive to predict the ultimate state of HSS joints accurately. The precise prediction of ductile fracture becomes very important in predicting the ultimate state and the post ultimate load behaviour of HSS structural members and welded joints. This paper focuses on the evaluation of existing data [2] to bring additional light to the behaviour of the S700 grade material.

The traditional elastoplastic hardening model may overestimate the plasticity's localisation effect in the necking zone if the material damage is not considered [3,4]. Diverse damage theories combining elastoplastic constitutive models have been developed to simulate the fracture initiation and propagation. Three main approaches classified from pioneering works are developed [5], namely the continuum damage model, the uncoupled damage model, and the micromechanics based damage model, to simulate the fracture of the material. The uncoupled damage model generally uses the equivalent plastic strain as an external variable uncoupled from the yield surface to govern the failure criteria. The material is damaged when the external variable reaches a critical value, as shown by several proposed models [6,7]. However, the parameter calibration process is firmly based on reliable experimental data. The continuum damage mechanics approach considers damage by correlating the damage with an internal variable. Lemaitre [8] proposed a damage model under the thermodynamics framework by modifying the Cauchy stress tensor to an effective stress tensor with a damage factor. Effective stress is used in the constitutive equation, indicating that the damage is coupled with the yield surface. The last approach is the micromechanics-based damage model. Under the framework of micromechanics damage models, the ductile fracture process could be described as the nucleation, growth, and coalescence of the microvoids [9]. The process initiates when the microvoids nucleate at inclusions or

* Corresponding author.
E-mail address: xinhaohui@xjtu.edu.cn (H. Xin).

https://doi.org/10.1016/j.jcsr.2021.106832
0143-974X/

second phase particles by particle-matrix interface de-cohesion or particle cracking. These voids grow and change the shape accompanying the plastic deformation of the matrix, and eventually, the microvoids coalesce resulting in the final failure of the material.

Several studies have shown that the Lode angle and the stress triaxiality are essential parameters for the ductile fracture [7,10–14]. The growth and coalescence of microvoids could explain the stress triaxiality and Lode angle dependency phenomenon at the microscale. At a high-stress triaxiality level, the voids grow volumetrically, and the necking of inter-void ligaments results in the coalescence of the voids [13]. On the other hand, the voids may grow, but the shear localisation at the inter-void ligaments governs the fracture initiation under a low-stress triaxiality. It demonstrates that the final fracture also depends on the Lode parameter, which represents the shear state of the material [13,14]. Gurson-Tvergaard-Needleman (GTN) Damage Model, as one of the most popular micromechanics-based porous plasticity models, links the macroscopic damage with the evolution of micro void volume fraction (VVF). It was initially proposed by Gurson [15], considering the growth of the voids only. Tvergaard [16,17] and Needleman and Tvergaard [18] improved the model by involving the void nucleation and coalescence. Furthermore, researches [19–23] have been done to extend the application range of the GTN model to the low-stress triaxiality state.

Generally, the effects of the stress triaxiality and the Lode Angle on failure modes and fracture properties could be investigated experimentally and numerically. A large number of specimens are required to identify the parameters of the damage model for each test series. Different types of coupon specimens such as smooth, notched bars, or compact tension specimens can be used to determine the fracture process [7,10–13,21]. However, it is difficult to conduct all kinds of reliable experiment to generate different stress states through different initial specimen geometries or by applying different load combinations for specific parts in the civil engineering sector, such as welds, HAZ, bolts, headed studs and fillet corners of cold-formed tube. Hence, the micromechanical analysis could be used as a surrogate model to numerically calibrate the ductile fracture parameters. Fritzen et al. [24] investigated the pressure dependency of the deviatoric limit stress of three-dimensional microstructures. The stress triaxiality is varied by applying different load conditions in addition to the periodic boundary condition. The GTN parameters for elastoplastic porous metals are identified using three-dimensional representative volume elements (3D RVE). Xin et al. [25] calibrated the material parameters of the orthotropic GTN model inferred from microstructures generated from the high-fidelity discrete element simulations. Xin et al. [26] calibrated the friction angle, the ratio of the yield stress in triaxial tension to the yield stress in triaxial compression, and the dilation angle of the linear Drucker-Prager plastic model based on the experimental result and the computational homogenisation.

In terms of the damage modelling of the cold-formed HSS, Pavlovic et al. [27] calibrated the damage model under the framework of the void growth model (VGM) for the HSS cold-formed material [28]. The FE prediction is generally agreed well with experimental observations, except that the resistance of FE results is larger than that of the test results at the descending stage. This is mainly because the fracture locus is not well considered at the lower stress triaxiality in the VGM model. Yan et al. [29] attempted to calibrate the GTN damage parameters for mild steel S355 based on the engineering stress-strain relationship. The 3D RVE is employed to determine the parameters q_1, q_2, and q_3 with constant values. A parametric study is carried out on the coupon simulation to calibrate VVF correlated parameters f_c and f_f.

In this paper, the GTN damage model is calibrated for the cold-formed S700 high strength steel under high-stress triaxiality. The experiment was conducted by Turan and Horvath [2] within the RUOSTE project [28]. The computational homogenisation method is employed to investigate the pressure dependency of the deviatoric stress. Different load conditions corresponding to different stress triaxiality levels are applied to eight unit cells, including random spherical pores, where VVF of eight unit cells varies from 0.1% to 30%. The parameters q_1, q_2, and q_3, which describe the yield surface of the material, are calibrated based on the inelastic deformation within the unit cell. An equation is proposed to describe the relationship between VVF and q_1 value. The parameters f_c and f_f are calibrated against the standard coupon test. Finally, the proposed parameters for the cold-formed S700 HSS are validated against the tensile tests for the specimens with a hole in the centre.

2. Theory background

2.1. GTN model

The GTN model involves nine constitutive parameters. Three constitutive parameters q_1, q_2, and q_3 are used to describe the shape of the yield surface. The other six parameters are employed to define the evolution of VVF. The yield surface of GTN model is presented in Eq. (1):

$$\phi = \left(\frac{\sigma_{eq}}{\sigma_y}\right)^2 + 2q_1 f^* \cosh\left(\frac{3q_2\sigma_m}{2\sigma_y}\right) - 1 - q_3 f^{*2} = 0 \tag{1}$$

where: σ_{eq}, $\sigma_{m,}$ and σ_y are the von Mises equivalent stress, the hydrostatic pressure, and the flow stress of the undamaged material matrix, respectively. The expressions for σ_{eq} and σ_m are given below:

$$\sigma_m = \frac{1}{3}\sigma_{ij}\delta_{ij} \tag{2}$$

$$\sigma_{eq} = \sqrt{\frac{3}{2}\left(\sigma_{ij} - \frac{1}{3}\sigma_{ij}\delta_{ij}\right)\left(\sigma_{ij} - \frac{1}{3}\sigma_{ij}\delta_{ij}\right)} \tag{3}$$

The evolution of VVF consists of the new void's nucleation and the growth of the existing void, see Eq. (4). The nucleation of the void may occur because of decohesion of the particle-matrix interface and microcracking. It follows a normal distribution regarding the equivalent plastic strain. Hence, the void nucleation rate involves three parameters: the total nucleated VVF f_n, the mean value of the normal distribution of the nucleation strain ε_n, and the standard deviation S_n. The expressions are given in Eqs. (5) and (6). The growth of the existing void is based on the law of conservation of mass. The rate of the void growth is expressed in terms of the plastic hydrostatic strain rate, as shown in Eq. (7). f^* is the modified VVF, a function of the critical VVF f_c and final VVF f_f. The evolution of VVF is accelerated and completed when VVF exceeds the f_c and reaches f_f, respectively. The expression is given in Eq. (8).

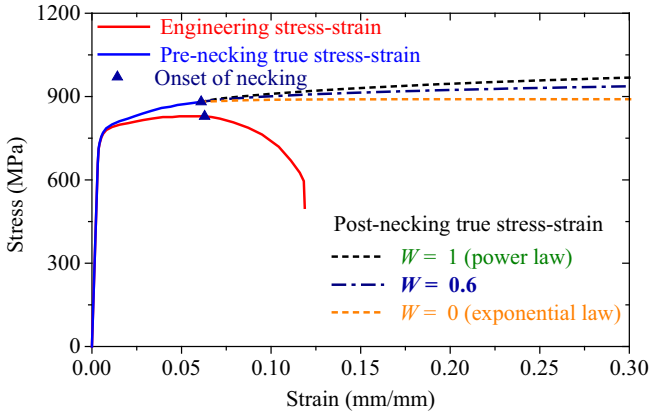

Fig. 1. Comparisons between engineering and true stress-strain of S700.

Table 1
Plasticity model parameters for S700.

E[GPa]	ν	A[MPa]	ε_0	n	k_0 [MPa]	Q [MPa]	β
210	0.3	1037.8	0.00499	0.0585	766.04	124.35	41.52

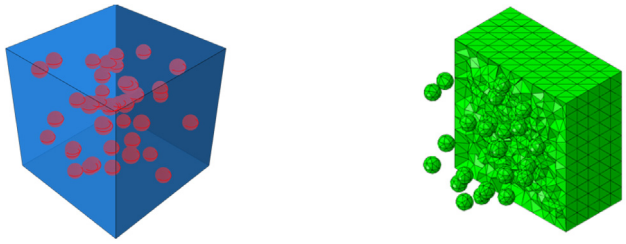

a) N=40, f=3%

b) N=80, f=10%

Fig. 2. Typical unit cell model with random voids.

Table 2
Details of microstructures.

f (%)	0.1	0.5	1.5	3	5	10	25	30
N	20	20	40	40	40	80	80	80
R (mm)	0.0229	0.0391	0.0447	0.0564	0.0668	0.0668	0.0907	0.0964
Elements	52,409	67,945	49,297	36,954	48,382	31,628	38,499	30,972

$$\dot{f} = \dot{f}_g + \dot{f}_n \tag{4}$$

$$\dot{f}_n = A\dot{\varepsilon}_{eq}^{pl} \tag{5}$$

$$A = \frac{f_n}{S_n\sqrt{2\pi}} e\left[-\frac{1}{2}\left(\frac{\hat{\varepsilon}_{eq}^{pl} - \varepsilon_n}{S_n}\right)^2\right] \tag{6}$$

$$\dot{f}_g = (1-f)\dot{\varepsilon}_{kk}^{pl} \tag{7}$$

$$f^* = \begin{cases} f & f < f_c \\ f_c + K(f - f_c) & f_c \le f < f_f \\ f_u^* & f \ge f_f \end{cases} \qquad K = \frac{f_u^* - f_c}{f_f - f_c} \tag{8}$$

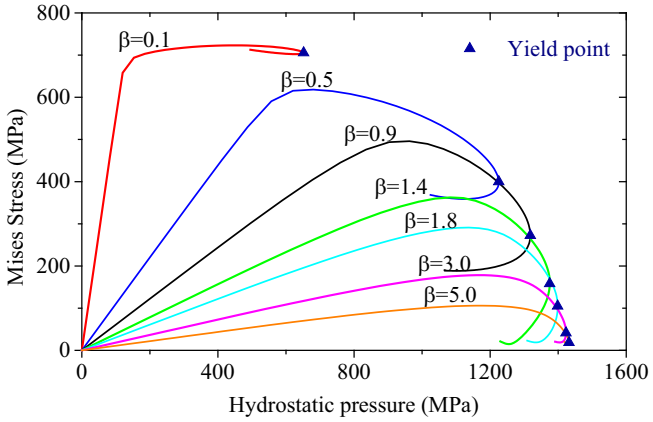

Fig. 3. Typical Mises stress-hydrostatic pressure relationship (f = 5%, α = 1, Exponential property).

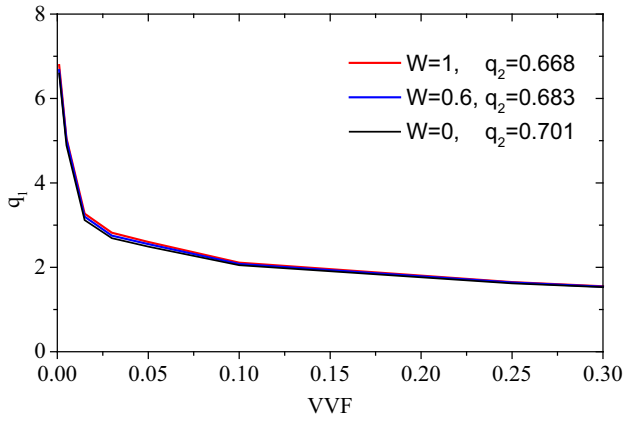

Fig. 4. Identified parameter q_1 regarding VVF.

Table 4
Identified parameters q_1 and q_2.

Property	W = 1 (Power law)		W = 0.6		W = 0 (Exponential law)	
VVF(%)	q_1	q_2	q_1	q_2	q_1	q_2
0.1	6.79	0.668	6.67	0.683	6.59	0.701
0.5	5.06		5.02		4.89	
1.5	3.27		3.20		3.12	
3	2.82		2.75		2.69	
5	2.60		2.55		2.49	
10	2.11		2.08		2.05	
25	1.65		1.64		1.62	
30	1.55		1.54		1.53	

2.2. Periodic boundary condition

The Hill-Mandel computational homogenisation method could establish the link between micro-scale and macro-scale behaviour.

Table 3
Parameters for different load conditions.

i	1	2	3	4	5	6	7	8	9	10	11	12	13
α	1	1	1	1	1	1	1	1	1	1	1	1	1
β	0.1	0.3	0.5	0.7	0.9	1.2	1.4	1.6	1.8	2.0	3.0	4.0	5.0

Table 5
Characterised parameters A and B.

Property	W = 1 (Power law)	W = 0.6	W = 0 (Exponential law)
A	1.144	1.133	1.119
B	−0.263	−0.262	−0.260

Table 6
Comparison of calibrated results and calculated results ($W = 0.6$).

Approach	Calibrated results	Calculated results	Scattering (%)
A	1.133	1.134	0.09
B	−0.262	−0.262	0.11
q_2	0.683	0.681	0.26

Fig. 5. Geometry of the coupon specimen.

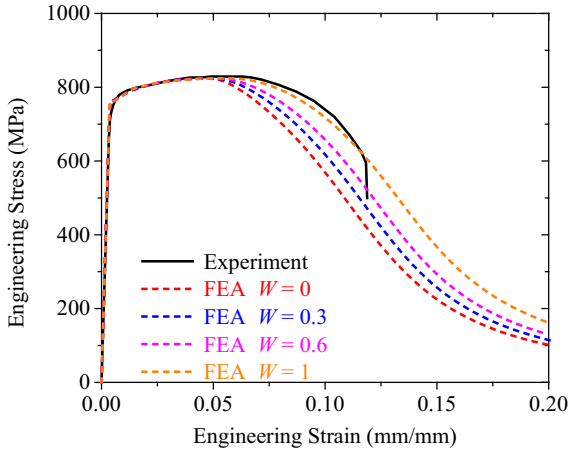

Fig. 6. Calibration of the weighting factor.

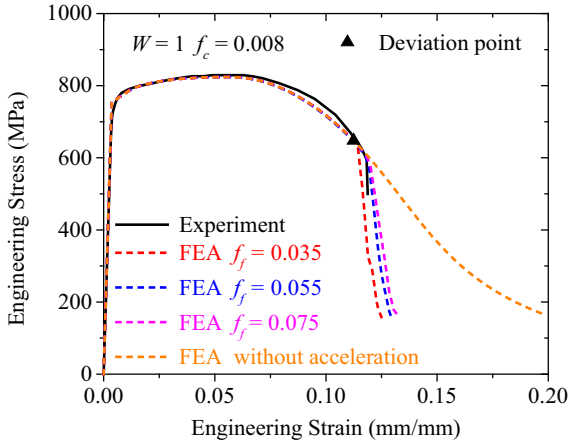

Fig. 7. Calibration of damage evolution.

Under the micro-scale level, the Cauchy stress $\tilde{\sigma}_{ij}$ in the unit cell domain could be upscaled to the Cauchy stress σ_{ij} in the macro-scale level by the following form [30]:

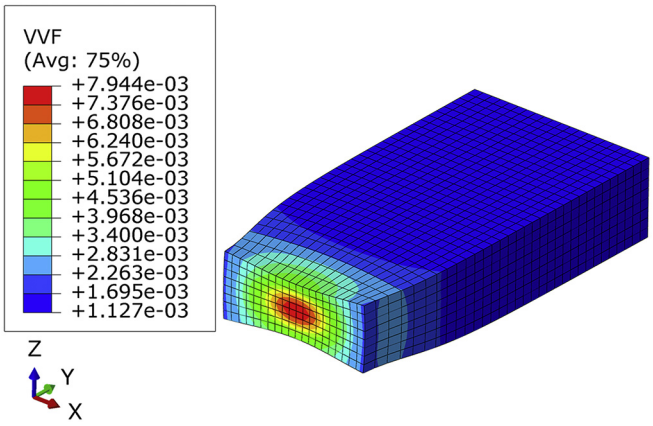

Fig. 8. Deformations and contour plots of VVF at deviation loading step.

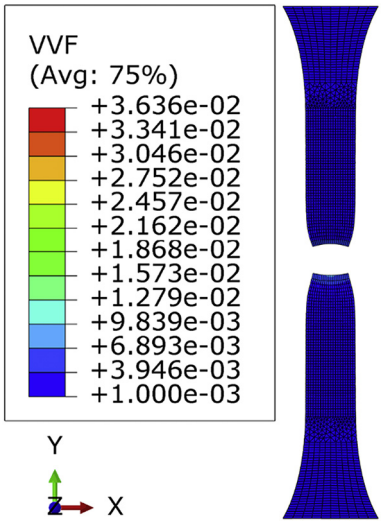

Fig. 9. Final failure of the model.

Table 7
Proposed parameters for the GTN model.

A	B	q_2	f_0	f_c	f_f
1.144	−0.263	0.668	0.001	0.008	0.055

$$\sigma_{ij} = \frac{1}{\Theta}\int_{\Theta} \tilde{\sigma}_{ij} d\Theta \tag{9}$$

where: $\tilde{\sigma}_{ij}$ is the micro-scale Cauchy stress, σ_{ij} is the macro-scale Cauchy stress, Θis the domain of the unit cell. The micro-scale displacement $u_i^f(x,y)$ is expressed in Eq. (10) [30]. It can be given by the leading order translation-free micro-scale displacement.

$$u_i^f(x,y) = \varepsilon_{ij}^c y_j + u_i^{(1)}(x,y) \tag{10}$$

where: $\varepsilon_{ij}^c$is the stain tensors in the macro-scale domain, $u_i^{(1)}(x,y)$ is the perturbation displacement of the micro-scale, x is the macro-scale position vector in the macro-scale domain, y is the micro-scale position vector in the unit cell domain.

The fine-scale displacement at a master node M and a slave node S, located on the opposite sides of the unit cell, is expressed as Eqs. (11) and (12).

Table 8
Measured dimensions and maximum resistance of specimens.

Specimen name	b [mm]	t [mm]	d_o [mm]	e_1 [mm]	e_2 [mm]	$F_{max\text{-}EXP}$ [kN]	$F_{max\text{-}FE}$ [kN]	Error [%]
S700/8 (B)	80.20	7.93	7.86	40.55	39.65	460.2	483.1	4.98
S700/16 (B)	80.11	7.91	15.85	40.36	39.75	405.5	427.9	5.52
S700/24 (B)	80.07	7.97	23.76	40.44	39.63	350.0	377.7	7.91
S700/32 (B)	80.11	7.86	31.87	40.39	39.72	302.0	319.4	5.76
S700/40 (B)	80.20	7.88	39.77	40.38	39.82	257.8	267.0	3.57

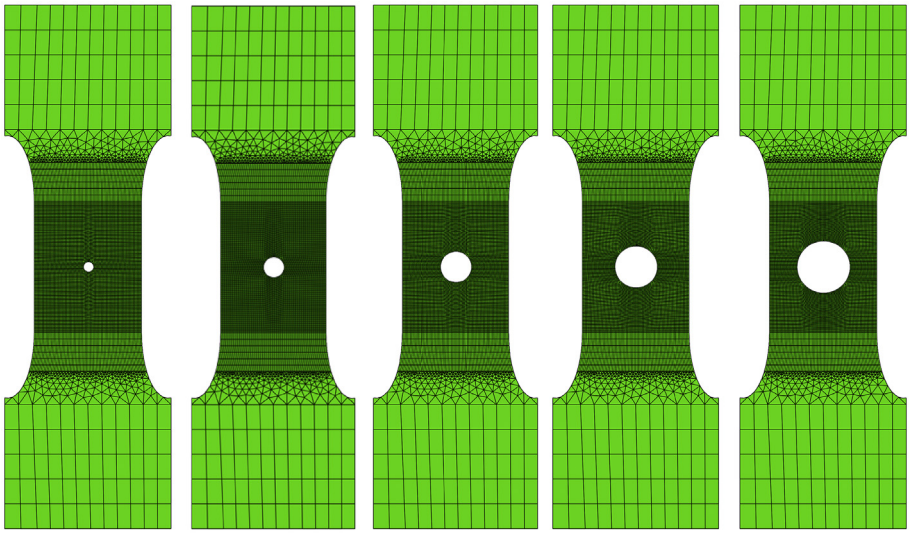

Fig. 10. Meshed model of notched coupon specimens (8 mm to 40 mm hole from left to right).

$$u_i^f(x, y^M) = \varepsilon_{ij}^c y_j^M + u_i^{(1)}\left(x, y_j^M\right) \tag{11}$$

$$u_i^f(x, y^S) = \varepsilon_{ij}^c y_j^S + u_i^{(1)}\left(x, y_j^S\right) \tag{12}$$

where: y^M and y^S are the fine-scale coordinates.

The periodic boundary condition on the unit cell requires the same perturbation displacement at M and S nodes. Hence, Eqs. (11) and (12) yield a constraint equation between the master node and the slave node, as expressed in Eq. (13).

$$u_i^f\left(x, y_j^M\right) - u_i^f\left(x, y_j^S\right) = \varepsilon_{ij}^c\left(y_j^M - y_j^S\right) \tag{13}$$

2.3. Uniaxial stress-strain relationship

The non-linear isotropic hardening model is employed to define the steel plasticity [31]. The full-range true stress-strain relationship consists of two parts: the pre-necking part and the post-necking part. The pre-necking true stress-strain relationship can be directly converted

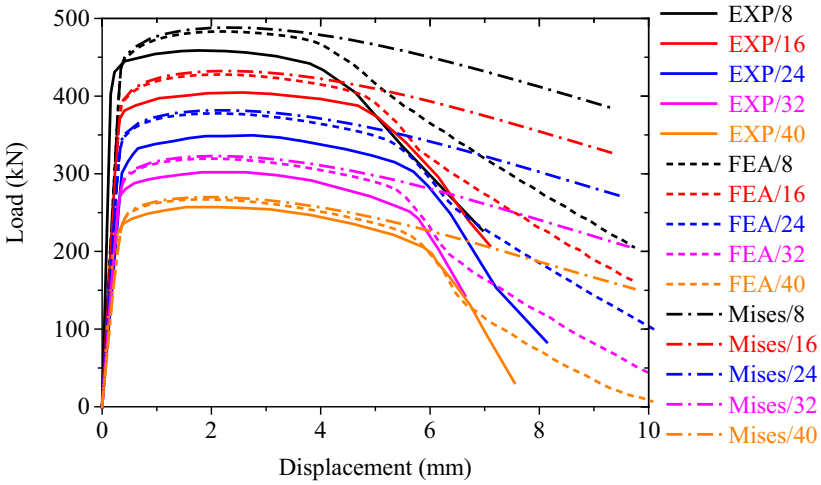

Fig. 11. Comparison of the load-deformation curves.

from the experimental engineering stress-strain curve, considering the law of conservation of mass and the assumption that the strain is uniformly distributed among all cross-sections within the measuring gauge length before necking. However, the post-necking true stress-strain relationship could not be directly inferred from the testing results due to the localisation of the plasticity. Hence, it is necessary to find an appropriate expression to describe the true stress-strain relationship after necking. A linear combination of power and exponential law [32] is employed to model the post-necking true stress-strain relationship in this paper, as expressed in Eq. (14). The power law (Swift model) [33] and the exponential law (Voce model) [34] are given in Eqs. (15) and (16), respectively. Besides, the initial necking condition Eq. (17) needs to be satisfied to determine the necking point.

$$\sigma_t[\bar{\varepsilon}_t] = W\sigma_S[\bar{\varepsilon}_t] + (1-W)\sigma_V[\bar{\varepsilon}_t] \tag{14}$$

$$\sigma_S[\bar{\varepsilon}_t] = A(\bar{\varepsilon}_t + \varepsilon_0)^n \tag{15}$$

$$\sigma_V[\bar{\varepsilon}_t] = k_0 + Q\left(1-e^{-\beta\bar{\varepsilon}_t}\right) \tag{16}$$

$$\left.\frac{d\sigma_t}{d\varepsilon_t}\right|_{\varepsilon_t=\varepsilon_{t,u}} = \sigma_{t,u} \tag{17}$$

where: W is the weighting factor; A, ε_0, n are the Swift parameters; k_0, Q, β are the Voce parameters; σ_t and ε_t are the true stress and the true strain; $\sigma_{t,u}$ and $\varepsilon_{t,u}$ are the true stress and true strain at the onset of necking, respectively.

3. Characterisation of the yield surface

3.1. Material property

The material property of the cold-formed S700 HSS is extracted from the standard dog-bone coupon test according to EN ISO 6892-1:2010 [35], as reported by Turan and Horvath [2]. The thickness of the coupon specimen is 8 mm. The pre-necking true stress-strain relationship is directly converted from the experimental engineering stress-strain relationship. The power law and the exponential law are fitted to the converted pre-necking data. The post-necking part is generated based on the extrapolation of the power and exponential law with a weighting factor. Fig. 1 depicts the engineering and true stress-strain relationships, including the post-necking part. The fitted parameters and the constitutive parameters are listed in Table 1.

3.2. Unit cell generation

Eight RVEs with different VVF f varying from 0.1% to 30% are employed to conduct computational homogenisation analysis. The cubic unit cell's side length is 1 mm, indicating that the volume of the unit cell is 1 mm^3. Non-overlapping voids with constant radius R are randomly scattered in the unit cell, as shown in Fig. 2. Fritzen et al. [24] carried out a convergence study to assure a sufficient quality of the results. Six different mesh refinement levels for the mesh density were investigated, and a medium-mesh density was suggested. In this study, a universal mesh size of 0.1 mm is used for all eight models, resulting in different numbers of elements presented in Table 2. The

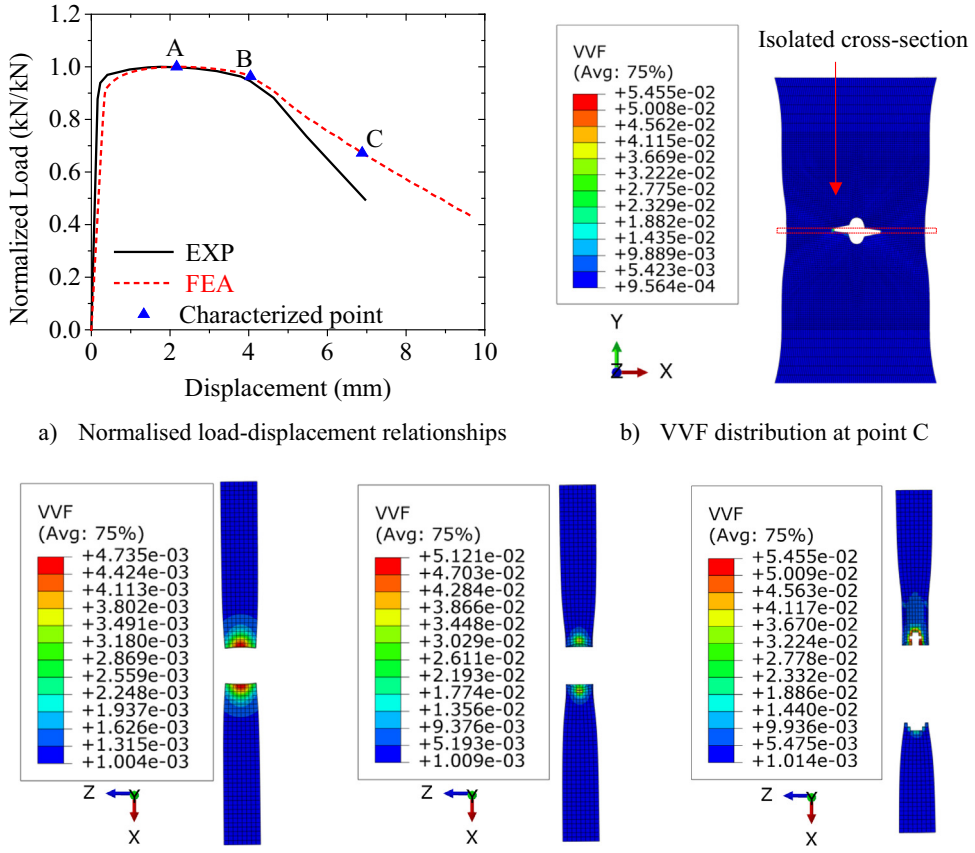

a) Normalised load-displacement relationships

b) VVF distribution at point C

c) VVF distribution of isolated cross section at point A, B, C

Fig. 12. 8 mm notched coupon specimen.

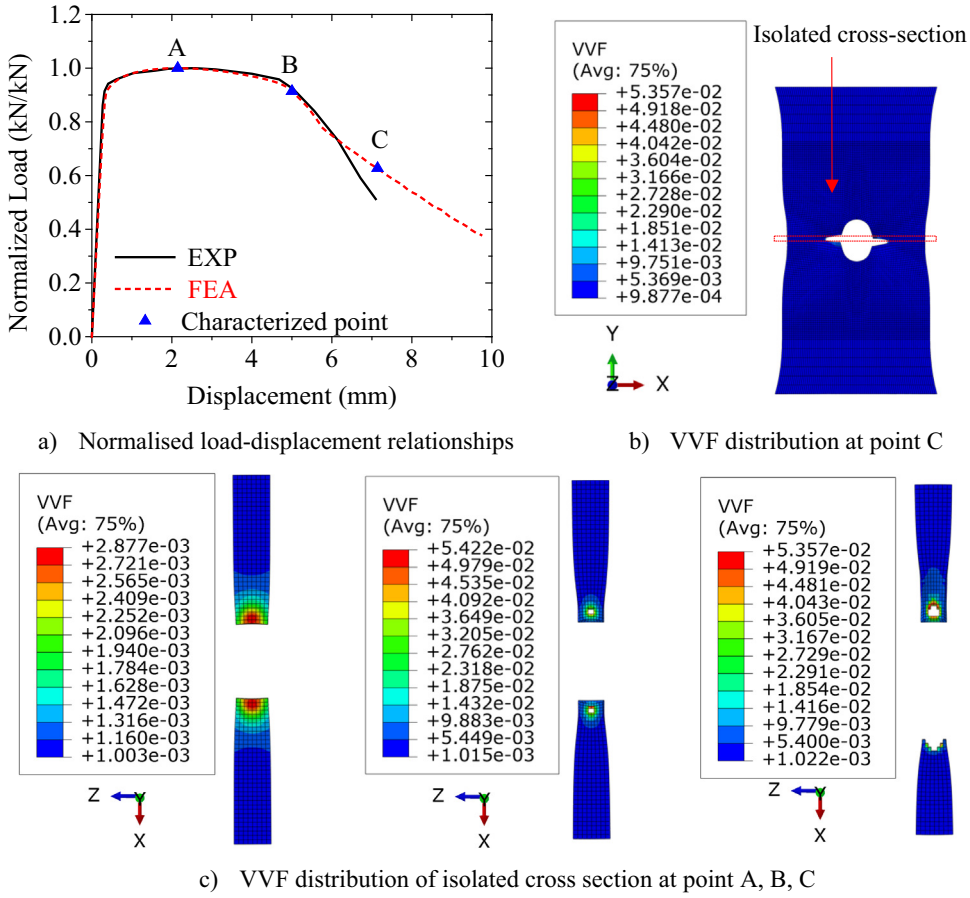

Fig. 13. 16 mm notched coupon specimen.

number of elements is greater than that proposed by Fritzen et al. [24]. In addition, the number of voids N, the radius R, and the porosity of the unit cell f are shown in Table 2. VVF f of the unit cell could be calculated according to Eq. (18).

$$f = \frac{4\pi R^3 N}{3|\Omega_{tot}|} \tag{18}$$

where: $|\Omega_{tot}|$ is the total volume of the unit cell.

3.3. Boundary conditions

The load is applied by imposing only the mean of the normal displacement on the surface of the unit cell. The strain–driven load is controlled by two parameters α and β proposed by Fritzen et al. [24], as expressed in Eq. (19). Thirteen load conditions, corresponding to thirteen hydrostatic pressure, are numerically tested to investigate the hydrostatic pressure dependency of the macroscopic yield surface. The detailed information of the parameters α and β are listed in Table 3.

$$\left[\dot{\bar{\varepsilon}}\right] = \alpha \begin{pmatrix} 1 & 0 & 0 \\ 0 & -1 & 0 \\ 0 & 0 & 0 \end{pmatrix} + \beta \begin{pmatrix} 1 & 0 & 0 \\ 0 & 1 & 0 \\ 0 & 0 & 1 \end{pmatrix} \tag{19}$$

3.4. Simulation results

Three hundred and twelve models are analysed in total, considering three material properties ($W = 0$, 0.6, and 1) depicted in Fig. 1, eight porous unit cell models shown in Table 2, and thirteen load conditions presented in Table 3. The Mises stress-hydrostatic pressure relationship is extracted from each model. An example including seven Mises stress-hydrostatic pressure curves from the model with 5% VVF and exponential material property is presented in Fig. 3. The yield point is characterised by the maximum hydrostatic pressure in each curve. It can be seen that the hydrostatic pressure has a negative contribution to the yield Mises stress.

3.4.1. Identification of parameters q_1, q_2, and q_3

Different values of the constitutive parameters q_1, q_2, and q_3 are proposed in literatures. $q_3 = q_1^2$ is suggested in the original GTN model. Based on the q_1 and q_3 relationship, the least-squares method is employed to fit the GTN model to the numerical result (the yield point shown in Fig. 3) by varying q_1 and q_2. Fritzen et al. [24] found a negative correlation between q_1 and VVF with a constant q_2. The conclusion also holds in this work.

The variables σ_{eq}, σ_m, σ_y, and f^* in Eq. (1) are determined based on the numerical data at the yield point for each model. σ_{eq} and σ_m equal to the Mises stress and the hydrostatic pressure, respectively. The flow stress σ_y is inferred based on the equivalent strain extracted from the model and the engineering stress-strain relationship. $f^*$is determined by the real VVF measured from the unit cell model. First, a constant q_2 is calibrated for each material property. Based on the constant q_2, q_1 is calibrated for eight VVFs. q_1 decreases with an increasing VVF and eventually yields around1.5, as shown in Fig. 4 and Table 4. It can be seen that a small difference, less than 5%, exists between the calibrated parameters for different material properties. A power law is employed, as expressed in Eq. (20), to describe the relationship between q_1 and VVF,

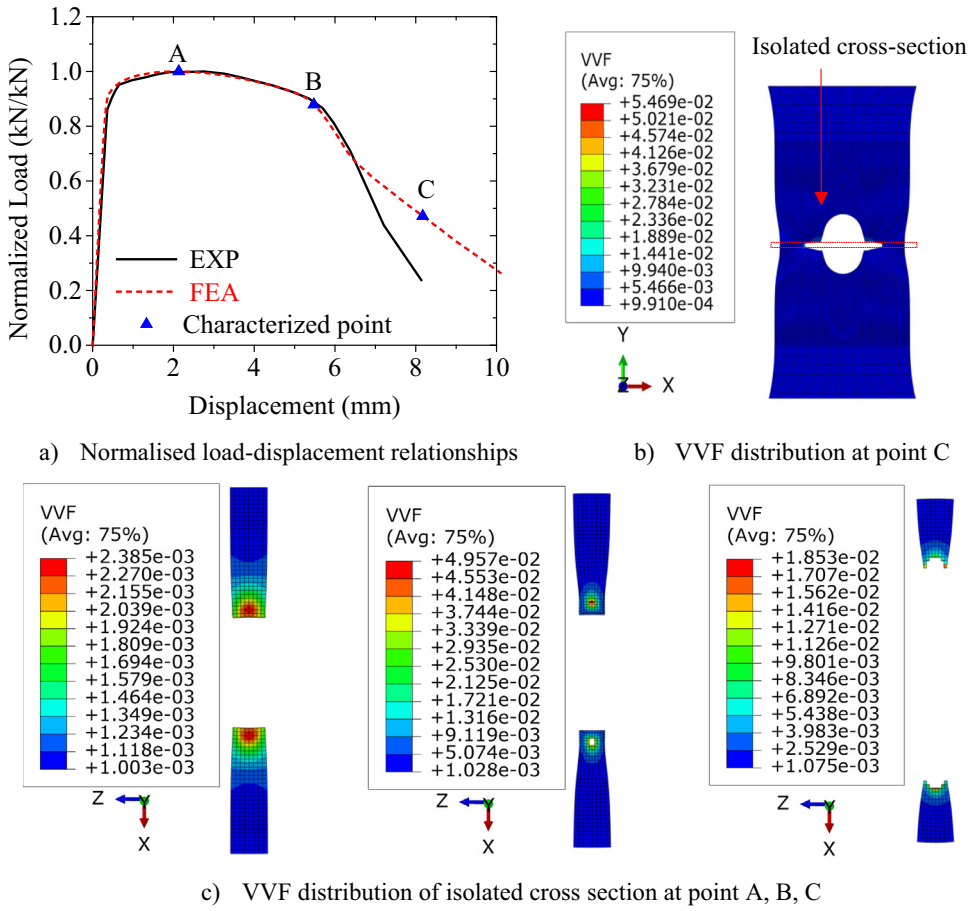

Fig. 14. 24 mm notched coupon specimen.

$$q_1 = A \cdot f^B \tag{20}$$

where: A and B are the constitutive parameters. The characterised value of A and B are presented in Table 5 for each material property.

3.4.2. Relation of the weighting factor and constitutive parameters

The computational homogenisation analysis is a very time-consuming process, considering the number of investigated VVFs and load conditions. Therefore, it is necessary to verify whether the weighting factor could be directly used to calculate the constitutive parameters q_1 (A, B) and q_2 based on the calibrated parameters using the exponential and the power constitutive models. The calculated parameters are compared to the calibrated parameters for material with a 0.6 weighting factor in Table 6. Given the maximum 0.26% deviation, it can be concluded that the assumption holds.

4. Parameters calibration for the standard coupon specimen

Standard tensile coupon tests were conducted according to EN ISO 6892-1:2010 [35], reported by Turan and Horvath [2]. The nominal plate thickness and width were 8 mm and 20 mm, respectively. The FE model is created based on the nominal dimension of the coupon specimen and analysed using the ABAQUS2019 package [31]. The meshed model is presented in Fig. 5. Note that the grip parts of the coupon specimen are not included in the model to improve computing efficiency. The MPC beam constraint is employed to constrain the end surface to a reference point at its centre by all degrees of freedom. The load is applied by a 20 mm displacement at RP2 in Y direction. The rest of the displacement at RP1 and RP2 is fully constrained. The explicit solver is used to perform quasi-static analysis on the coupon test. The period in the loading step is set to 100 s and the target time increment is 0.0001 s. The non-linear properties are used in the explicit model, making the numerical analysis sensitive to the mesh size. Therefore, it is necessary to have a fine mesh in the fracture region. For the less important part, a coarse mesh is used considering the efficiency of the calculation. The tetrahedral C3D10M element is used for the transition part, connecting the fine mesh part and the coarse mesh part. Eight node hexahedral solid element (C3D8) with 1 mm mesh size is used in the parallel part. Mesh convergency studies were carried out for structural steels under monotonic and quasi-static tensile loading in many literatures [36,37]. The mesh size in the critical region varied from 1 mm to 0.05 mm. However, as the final goal of this research series is to implement the GTN damage model on welded X-joints made of HSS hollow sections, it is crucial to use the same mesh size in the critical region of X-joints and the parallel part of the coupon specimen. Considering the dimension of X-joints, the FE analysis on X-joints would be time-consuming if a mesh size smaller than 1 mm is used. Therefore, the 1 mm mesh size is accepted for the damage modelling of the critical regions of coupon specimens and welded joints [38].

As stated before, the tensile behaviour of the coupon specimen could be well predicted up to the necking point. After the necking point, the critical cross-section starts to lose resistance due to the nucleation, growth, and coalescence of the void, although the true stress of the undamaged material might continuously increase. The calibration process is proceeded by comparing the FE and experimental engineering stress-strain relationship. The FE engineering stress-strain relationship is obtained by analysing the elongation of the gauge length and the reaction force at the reference point. The post-necking part of the experimental engineering stress-strain relationship is fitted by varying the weighting

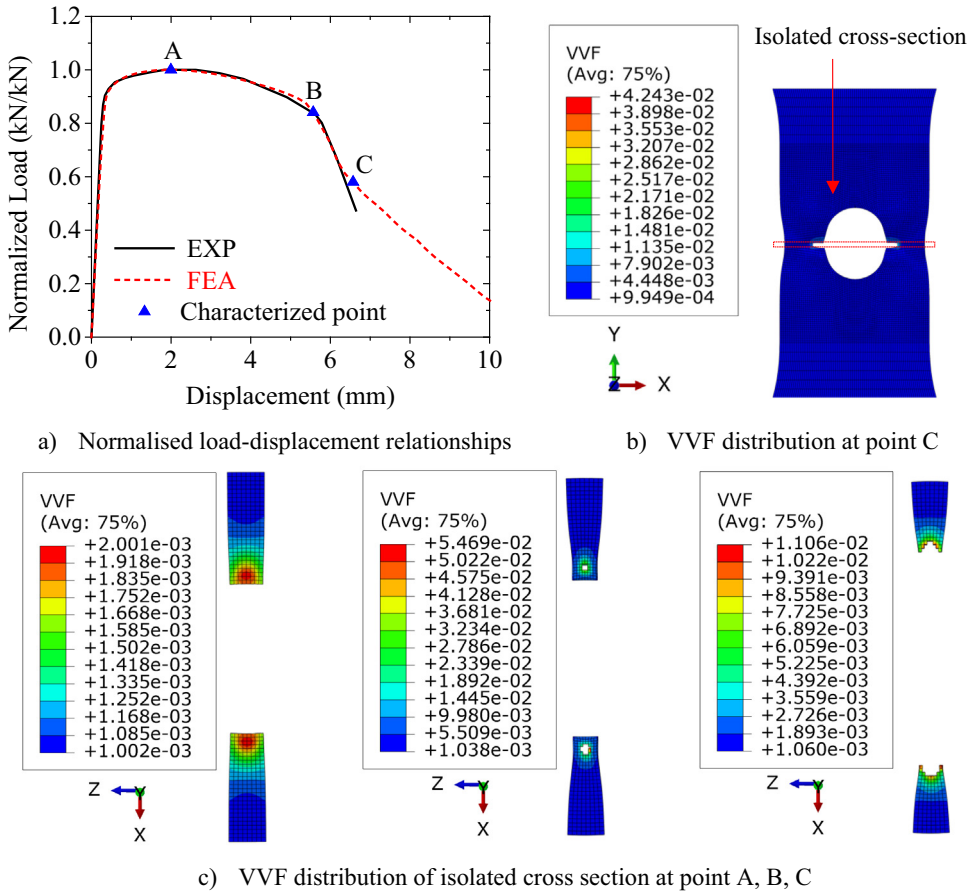

Fig. 15. 32 mm notched coupon specimen.

factor. Based on the determined weighting factor, the critical VVF f_c and final VVF f_f that govern the acceleration of VVF evolution are calibrated. Note that the nucleation of the void is not involved in the current research.

4.1. Calibration of the weighting factor

Different true stress-strain relationships, including the pre-necking and the post-necking parts, are introduced in Fig. 1. The post-necking part is generated based on the extrapolation of the power law and the exponential law by using the weighting factor. The isotropic hardening plasticity is used in the form of the true stress-plastic strain relationship in ABAQUS. The porous metal plasticity is employed to consider the pressure-dependence yield surface of the GTN model. The relationship between q_1 and VVF is realised by using a user subroutine VUSDFLD provided in Appendix A. The initial VVF is set to 0.001, indicating that the relative density is 0.999. Note that only the growth of the void is considered at the phase of weighting factor calibration.

The engineering stress-strain relationships extracted from FEMs are compared to the experimental result in Fig. 6. Four weighting factors 0, 0.3, 0.6, and 1 are investigated. With a larger weighting factor, the engineering stress decreases slower in the post-necking part. A good agreement could be observed between the result with the largest weighting factor (the power law) and the experimental result.

4.2. Calibration of the parameters f_c and f_f

The damage evolution is investigated based on the determined weighting factor. According to Eq. (8), VVF is enlarged by two parameters, the critical VVF f_c and the final VVF f_f, with linear interpolation. The VVF evolution acceleration starts when VVF reaches f_c and ends when VVF reaches f_f under the microscale level. In the modelling of the coupon test, the acceleration of VVF is introduced at the loading step when the FE engineering stress-strain curve starts to deviate from the experimental curve. It is observed that the deviation of the FE result starts when the stress decreases to approximately 650 MPa, as shown in Fig. 7. Fig. 8 depicts the VVF contour plot in the necking region at the loading step corresponding to the stress deviation. The maximum VVF, which is almost 0.008, appears at the centre of the cross-section. Hence, 0.008 is adopted for f_c in the following calibration process.

f_f is determined by testing different values in the FEM. Three FE curves are compared to the experimental data in Fig. 7. It can be seen that the failure appears earlier if a smaller f_f is used since the material completely lose strength when f_f is reached. The model with $f_f = 0.055$ shows the best result compared to the experimental data. The final failure of the model is shown in Fig. 9. The element is deleted from the FE model when f_f is reached. The calibrated parameters for the cold-formed high strength steel S700 are proposed in Table 7, based on the parametric study.

5. Validation against notched coupon specimens

The calibrated GTN model, using the parameters presented in Table 7, is verified against five notched coupon tests (S700 (B) series) reported by Turan and Horvath [2]. The notched coupon specimen has a circular hole in the centre. The nominal diameter of the hole varies from 8 mm to 40 mm with an 8 mm interval. The stress triaxiality has a significant influence on the yield surface of the material, as explained earlier. By varying the diameter of the hole in the specimen, the influence of the high-stress triaxiality, higher than 0.33, on the yield surface

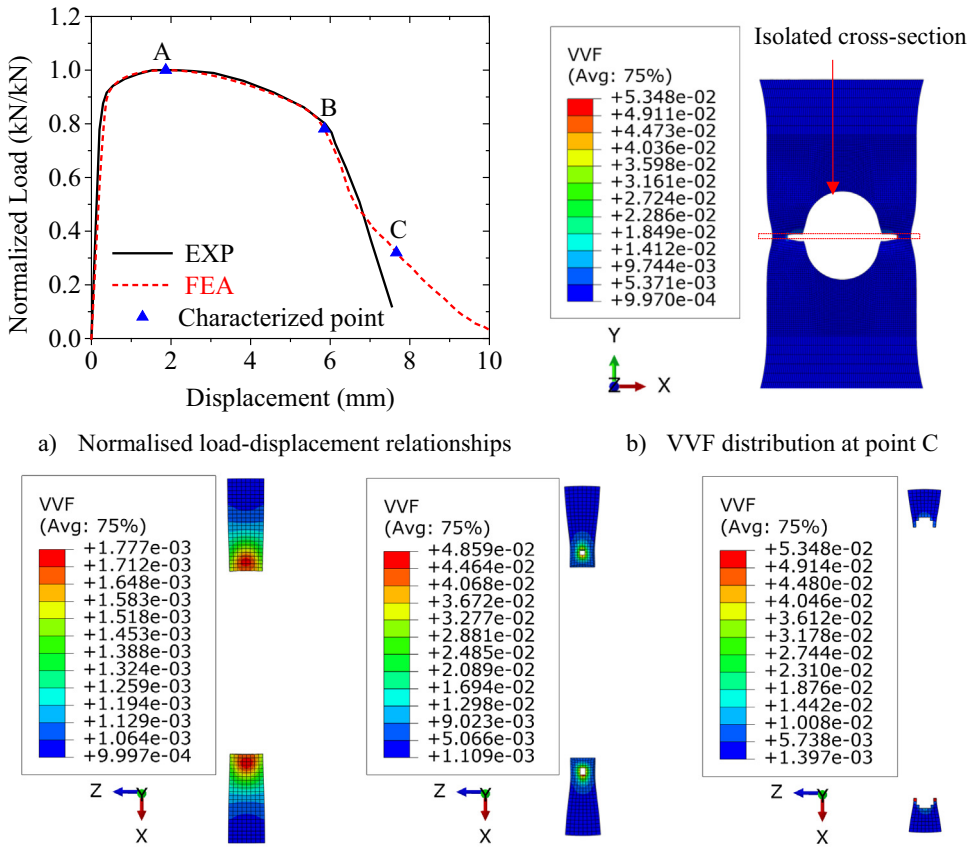

Fig. 16. 40 mm notched coupon specimen.

Table 9
Comparison of the fracture initiation point.

Specimen name	Displacement			Normalised force		
	EXP [mm]	FE [mm]	Deviation [%]	EXP [kN/kN]	FE [kN/kN]	Deviation [%]
S700/8 (B)	4.05	4.04	−0.04	0.95	0.96	1.93
S700/16 (B)	5.04	5.00	−0.72	0.92	0.91	−0.81
S700/24 (B)	5.69	5.48	−3.82	0.87	0.88	1.46
S700/32 (B)	5.79	5.57	−3.72	0.80	0.84	4.90
S700/40 (B)	5.88	5.85	−0.37	0.80	0.78	−2.32

could be investigated experimentally. The measured dimension and the original name of the notched specimen are listed in Table 8, where b is the width of the parallel part, t is the thickness, d_0 is the diameter of the hole, e_1 and e_2 are the distance from the centre of the hole to the two edges of the specimen. FEMs are employed to simulate the tensile performance of the notched coupon specimen. The measured dimension is used in FEM. The same basic setting and parameter introduced for simulating standard coupon test are used to simulate the notched coupon tests. The meshed FE models are shown in Fig. 10. The mesh size used for the parallel part of the notched specimen is identical to that of the standard coupon specimen (1 mm mesh size in the parallel part) to avoid the mesh size effect. Comparing the FE result to the experimental result, the interaction of the hydrostatic stress and the Mises yield stress of the calibrated GTN model could be verified.

The FE and experimental load-deformation relationships are compared in Fig. 11. The ultimate resistance of the FE result is averagely 5.7% higher than the experimental result, as shown in Table 8. The discrepancy may result from two possible reasons, which are the effect of stress triaxiality and the effect of loading rate.

Yan-Bo Wang et al. [39] and Yuan-Zuo Wang et al. [37] conducted a comprehensive experimental and numerical investigation on the yield criterion and the damage model of HSS. It was found that the influence of high-stress triaxiality (greater than 0.33) on the Mises plasticity model of HSS is negligible, while the stress triaxiality plays a crucial

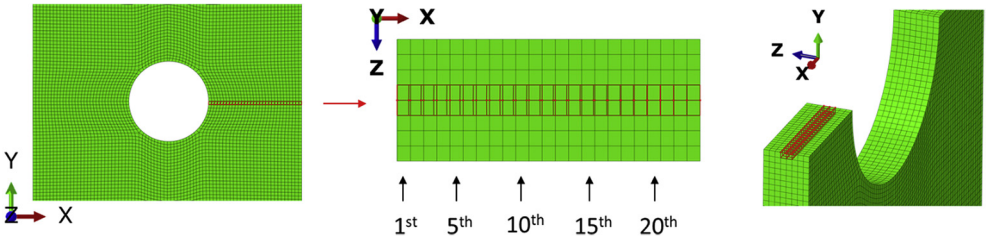

Fig. 17. Position of the investigated elements.

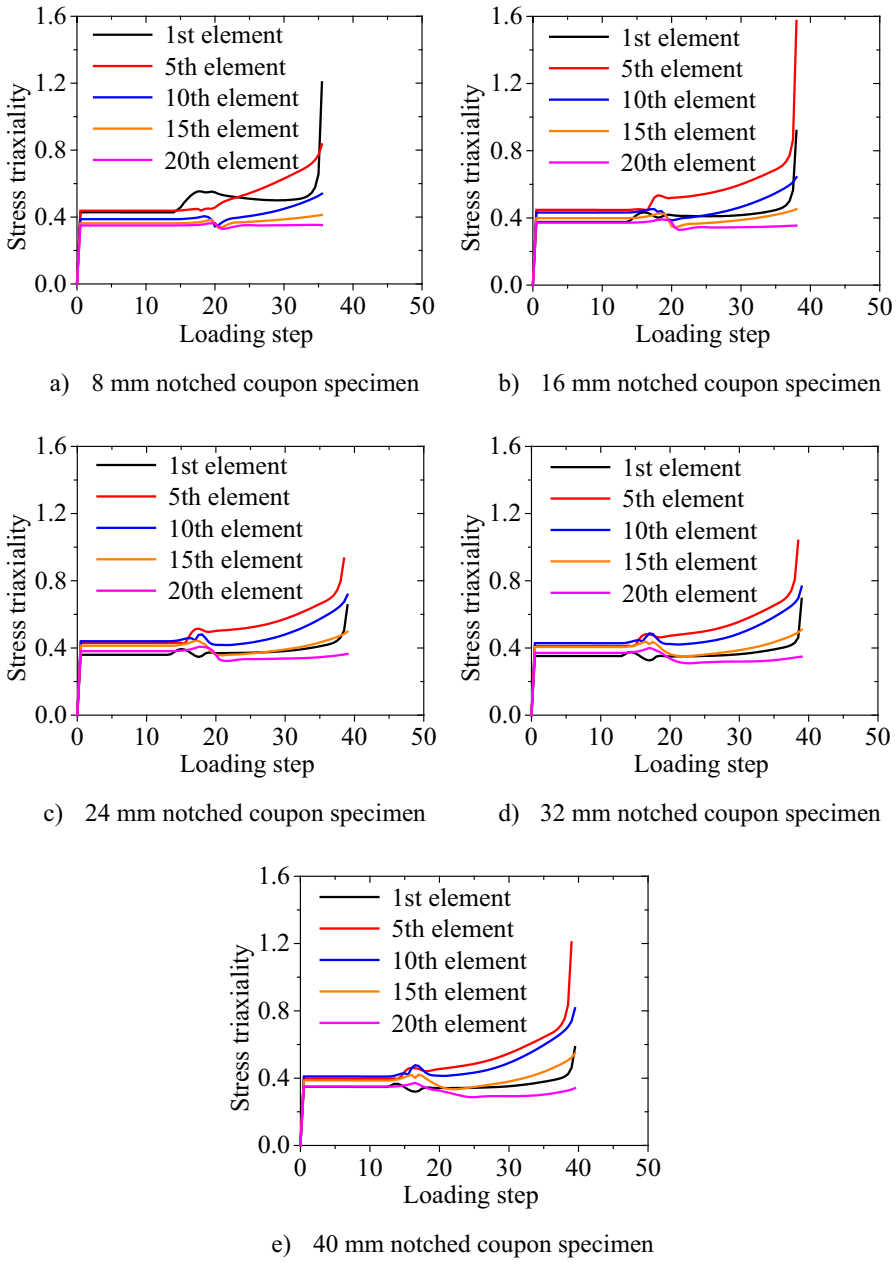

Fig. 18. Stress triaxiality versus loading step relationships.

role in the damage model. Therefore, based on the determined undamaged stress-strain relationship (W = 1, following the power law), the Mises yield criterion is employed in the FEMs to verify the influence of stress triaxiality. The results are plotted in Fig. 11. It can be seen that the results using the Mises yield criterion fit the results using the GTN damage model well with 1% maximum resistance discrepancy, indicating that the higher resistance predicted by the FEM is not due to the effect of stress triaxiality.

In the investigated testing series, the loading rate for the standard coupon specimen was higher than the notched coupon specimen, indicating that a higher material strength is obtained from the standard coupon test due to the strain rate effect. It is, therefore, reasonable to obtain a higher ultimate resistance in the FEM than the experiment. In order to eliminate the strain rate effect, the displacement of the stroke should be held for at least 60 s during the coupon test [40]. A static stress is obtained from each loading suspension point. Then, the static stress-strain relationship from the standard coupon test and the static load-displacement relationship from the notched coupon test are obtained based on several static stress points. Finally, the static behaviour of the standard and the notched coupon tests are predicted using the static stress-strain relationship obtained from the standard coupon test. And the strength deviation in Fig. 11, due to the strain rate effect, could be eliminated. However, the standard coupon test and the notched coupon test were conducted without the loading suspension [2]. Consequently, it is not possible to eliminate the strain rate effect in the FE analysis. In order to compare the FE and the experimental results focusing on the post ultimate load behaviour, the load is normalised by the maximum load, respectively. Therefore, the maximum normalised load of each curve is 1. Note that the displacement is not normalised.

The normalised load-displacement relationships for each test are depicted in Fig. 12 - Fig. 16. It can be seen that very good agreements exist between the FE and the experimental results. Three points are characterised in the FE result. The points A, B, and C correspond to the maximum load, the initiation of the fracture, and the largest

deformation in the experiment, respectively. The fracture initiation happens when the first element deletion is observed in the critical net cross-section in FEM. VVF contour plot of the isolated net cross-section at each characterised point is shown in Fig. 12 - Fig. 16. It can be seen that VVF at the centre of the cross-section develops faster than the edge. Consequently, the fracture initiates from the centre and grows to the edge. The maximum VVF in all figures is lower than the final VVF f_f, because the element is deleted from the model if f_f is reached. The displacement and the normalised load at the fracture initiation point B are compared to the experimental result at the point when the load starts to drop significantly in Table 9. The average deviation of the displacement and the normalised load is −1.7% and 1.0%, respectively. It can be concluded that the calibrated GTN model could effectively predict the damage initiate point under different stress triaxialities. The validated up limit of the stress triaxiality is investigated based on the average stress triaxiality extracted from elements in the central two layers of the net cross section. The 1st, 5th, 10th, 15th, and 20th elements from the hole edge, as shown in Fig. 17, are employed to demonstrate the stress triaxiality level during the loading. The stress triaxiality is plotted against the loading step for each model in Fig. 18. The relationship is plotted up until the characterised fracture initiation point B. From Fig. 18, it can be concluded that the validated maximum stress triaxiality is around 1.6.

To summarise, the behaviour of the notched coupon specimens could be well predicted by using the calibrated GTN model. The validated range of stress triaxiality is up to 1.6.

6. Conclusions and future work

The Gurson-Tvergaard-Needleman (GTN) damage model is calibrated for the S700 cold-formed high strength steel (HSS). The undamaged material property is generated based on a linear combination of the Swift model and the Voce model. The computational homogenisation analysis is conducted to identify the constitutive parameters q_1, q_2, and q_3, based on different undamaged material properties. A user subroutine (Appendix A) that realises the q_1-VVF relationship is implemented in ABAQUS2019 software packages. Based on the determined constitutive parameters and the undamaged material property, the damage evolution parameters f_c and f_f are calibrated. Finally, the calibrated GTN model is verified against five notched coupon tests. Very good agreements are observed between the FE and experimental results. The following conclusions are drawn.

1. A negative correlation between q_1 and VVF f, $q_1 = A \cdot f^B$, is found considering a constant q_2.
2. The parameters A and B are calibrated based on the computational homogenisation result. Additionally, the weighting factor used for generating the undamaged material property could be directly used to calculate the parameters A and B by doing a linear interpolation based on the calibrated parameters for the Swift model and the Voce model. The maximum deviation is 0.26%.
3. The undamaged material property following the power law (W = 1) fits the experimental data best. The calibrated parameters of the GTN model are shown in Table 7.
4. The calibrated GTN model could efficiently predict the behaviour of the notched coupon specimens. The average deviation of the displacement and the normalised load at the fracture initiation point is −1.7% and 1.0%, respectively. The validated range of stress triaxiality is up to 1.6.

The following three tasks are out of the scope of this paper and will be accomplished soon:

(1) The applicable range regarding the stress triaxiality will be extended to a lower stress state to model the shear failure;
(2) The GTN damage model, validated for the high-stress and low-stress triaxialities, will be calibrated for the base material and the heat affected zone of welded cold-formed HSS hollow sections;
(3) The calibrated GTN model will be used in the damage modelling of welded X-joints made of cold-formed HSS hollow sections.

Declaration of Competing Interest

The authors declare that they have no known competing financial interests or personal relationships that could have appeared to influence the work reported in this paper.

Appendix A

```
      subroutine vusdfld(
c Read only -
     *   nblock, nstatev, nfieldv, nprops, ndir, nshr,
     *   jElem, kIntPt, kLayer, kSecPt,
     *   stepTime, totalTime, dt, cmname,
     *   coordMp, direct, T, charLength, props,
     *   stateOld,
c Write only -
     *   stateNew, field )
c
      include 'vaba_param.inc'
c
      dimension jElem(nblock), coordMp(nblock,*),
     *          direct(nblock,3,3), T(nblock,3,3),
     *          charLength(nblock), props(nprops),
     *          stateOld(nblock,nstatev),
     *          stateNew(nblock,nstatev),
     *          field(nblock,nfieldv)
      character*80 cmname
c
      parameter(nrData=6,RPI=3.141592653D0)
      character*3 cData(maxblk*nrData), jData(maxblk*nrData)
      dimension rStrainData(maxblk*nrData)
      dimension strain(nblock,nrData)

C Parameters used in the simulation
C ######################################################################
      RVVFINITIAL = 0.001              ! Initial void volume fraction
      RVVFINITIALC = 0.008             ! fc
      RVVFFINALC =  0.055              ! ff
      RA = 1.144                       ! Paramters to calculate Q1
      RB = -0.263                      ! Parameters to calculate Q1
      RQ2 = 0.668                      ! Parameter Q2
C ######################################################################
c
      jStatus = 1
      call vgetvrm( 'PE', rStrainData, jData, cData, jStatus )
      strain = reshape(rStrainData,(/ nblock,nrData/))
c
      if( jStatus .ne. 0 ) then
        field(k,1) = RVVFINITIAL
        call xplb_abqerr(-2,'Utility routine VGETVRM '//
     *     'failed to get variable.',0,zero,' ')
        call xplb_exit
      end if
```

```
      do k = 1, nblock
      PE11_OLD =  stateOld(k,1)
      PE22_OLD =  stateOld(k,2)
      PE33_OLD =  stateOld(k,3)

      stateNew(k,1) =  strain(k,1)
      stateNew(k,2) =  strain(k,2)
      stateNew(k,3) =  strain(k,3)

      PE11INC = strain(k,1) - PE11_OLD
      PE22INC = strain(k,2) - PE22_OLD
      PE33INC = strain(k,3) - PE33_OLD

      IF(stateOld(k,4) .GT. 0.0) THEN
      stateNew(k,4) = stateOld(k,4) + (1 - stateOld(k,4))*(PE11INC +
     1            PE22INC + PE33INC)
      ELSE
      stateNew(k,4) = RVVFINITIAL
      ENDIF


      RQ1 = RA*(field(k,1))**RB
      RQ3 = RQ1**2.0
      RVOIDFAILURE = (RQ1 + SQRT(RQ1**2.0-RQ3))/RQ3

      IF (field(k,1) .GT. RVOIDFAILURE)  THEN
      stateNew(k,5) = 0.0
      ELSE
      stateNew(k,5) = 1.0
C DEFINE THE VOLUME FRACTION

      IF(stateNew(k,4) .LT. RVVFINITIALC) THEN
      field(k,1) = stateNew(k,4)
      ELSE IF (stateNew(k,4) .GT. RVVFFINALC) THEN
      field(k,1) = RVOIDFAILURE
      ELSE
      field(k,1) = RVVFINITIALC + (RVOIDFAILURE - RVVFINITIALC) /(
     1   RVVFFINALC-RVVFINITIALC)*(stateNew(k,4)-RVVFINITIALC)
      ENDIF

      ENDIF
      end do

      return
      end
```

(*continued*).

References

[1] Eurocode EC, 3: Design of Steel Structures Part 1–12: Additional Rules for the Extension of EN 1993 up to Steel Grades S700[R]. EN 1993-1-12, 2007.
[2] P. Turán, L. Horváth, Experimental behaviour of tension plates with centre hole made from high strength steel, Nordic Steel Construction Conference 2015 Tampere, Finland, 2015.
[3] K.S. Zhano, Z.H. Li, Numerical analysis of the stress-strain curve and fracture initiation for ductile material, Eng. Fract. Mech. 49 (1994) 235–241, https://doi.org/10.1016/0013-7944(94)90006-X.
[4] Y. Ling, Uniaxial true stress-strain after necking, AMP J. Technol. 5 (2004) 37–48.
[5] T.S. Cao, Models for ductile damage and fracture prediction in cold bulk metal forming processes: a review, Int. J. Mater. Form. 10 (2017) 139–171, https://doi.org/10.1007/s12289-015-1262-7.
[6] J.R. Rice, D.M. Tracey, On the ductile enlargement of voids in triaxial stress fields*, J. Mech. Phys. Solids. 17 (1969) 201–217, https://doi.org/10.1016/0022-5096(69)90033-7.
[7] Y. Bai, T. Wierzbicki, A new model of metal plasticity and fracture with pressure and lode dependence, Int. J. Plast. 24 (2008) 1071–1096, https://doi.org/10.1016/j.ijplas.2007.09.004.
[8] J. Lemaitre, A continuum damage mechanics model for ductile fracture, Int. J. Press. Vessel. Pip. 107 (1985) 335–344, https://doi.org/10.1016/S0308-0161(00)00019-3.
[9] A.A. Benzerga, J.B. Leblond, Ductile Fracture by Void Growth to Coalescence, Elsevier Inc., 2010https://doi.org/10.1016/S0065-2156(10)44003-X.
[10] R. Kiran, K. Khandelwal, Experimental studies and models for ductile fracture in ASTM A992 steels at high triaxiality, J. Struct. Eng. 140 (2014).
[11] G. Mirone, D. Corallo, A local viewpoint for evaluating the influence of stress triaxiality and lode angle on ductile failure and hardening, Int. J. Plast. 26 (2010) 348–371, https://doi.org/10.1016/j.ijplas.2009.07.006.
[12] X. Gao, T. Zhang, J. Zhou, S.M. Graham, M. Hayden, C. Roe, On stress-state dependent plasticity modeling: significance of the hydrostatic stress, the third invariant of stress deviator and the non-associated flow rule, Int. J. Plast. 27 (2011) 217–231, https://doi.org/10.1016/j.ijplas.2010.05.004.
[13] I. Barsoum, J. Faleskog, Rupture mechanisms in combined tension and shear-experiments, Int. J. Solids Struct. 44 (2007) 1768–1786, https://doi.org/10.1016/j.ijsolstr.2006.09.031.
[14] K. Danas, P. Ponte Castañeda, Influence of the lode parameter and the stress triaxiality on the failure of elasto-plastic porous materials, Int. J. Solids Struct. 49 (2012) 1325–1342, https://doi.org/10.1016/j.ijsolstr.2012.02.006.
[15] A.L. Gurson, Continuum theory of ductile rupture by void nucleation and growth: part I—yield criteria and flow rules for porous ductile media, J. Eng. Mater. Technol. 99 (1977) 2–15, https://doi.org/10.1115/1.3443401.
[16] V. Tvergaard, Influence of void nucleation on ductile shear fracture at a free surface, J. Mech. Phys. Solids. 30 (1982) 399–425, https://doi.org/10.1016/0022-5096(82)90025-4.
[17] V. Tvergaard, Ductile fracture by cavity nucleation between larger voids, J. Mech. Phys. Solids. 30 (1982) 265–286, https://doi.org/10.1016/0022-5096(82)90033-3.
[18] V. Tvergaard, A. Needleman, Analysis of the cup-cone fracture in a round tensile bar, Acta Metall. 32 (1984) 157–169, https://doi.org/10.1016/0001-6160(84)90213-X.
[19] K. Nahshon, J.W. Hutchinson, Modification of the Gurson model for shear failure, Eur. J. Mech. A Solids. 27 (2008) 1–17, https://doi.org/10.1016/j.euromechsol.2007.08.002.
[20] K.L. Nielsen, V. Tvergaard, Ductile shear failure or plug failure of spot welds modelled by modified Gurson model, Eng. Fract. Mech. 77 (2010) 1031–1047, https://doi.org/10.1016/j.engfracmech.2010.02.031.
[21] M. Achouri, G. Germain, P. Dal Santo, D. Saidane, Experimental characterization and numerical modeling of micromechanical damage under different stress states, Mater. Des. 50 (2013) 207–222, https://doi.org/10.1016/j.matdes.2013.02.075.
[22] M. Achouri, G. Germain, P. Dal Santo, D. Saidane, Numerical integration of an advanced Gurson model for shear loading: application to the blanking process, Comput. Mater. Sci. 72 (2013) 62–67, https://doi.org/10.1016/j.commatsci.2013.01.035.
[23] L. Malcher, F.M. Andrade Pires, J.M.A. César De Sá, An extended GTN model for ductile fracture under high and low stress triaxiality, Int. J. Plast. 54 (2014) 193–228, https://doi.org/10.1016/j.ijplas.2013.08.015.
[24] F. Fritzen, S. Forest, T. Böhlke, D. Kondo, T. Kanit, Computational homogenization of elasto-plastic porous metals, Int. J. Plast. 29 (2012) 102–119, https://doi.org/10.1016/j.ijplas.2011.08.005.
[25] H. Xin, J.A.F.O. Correia, M. Veljkovic, F. Berto, Fracture parameters calibration and validation for the high strength steel based on the mesoscale failure index, Theor. Appl. Fract. Mech. 112 (2021) https://doi.org/10.1016/j.tafmec.2021.102929.
[26] H. Xin, M. Veljkovic, J.A.F.O. Correia, F. Berto, Ductile fracture locus identification using mesoscale critical equivalent plastic strain, Fatigue Fract. Eng. Mater. Struct. 44 (2021) 1292–1304, https://doi.org/10.1111/ffe.13429.
[27] M. Pavlović, P. Manoleas, M. Veljkovic, E. Koltsakis, Calibration of the Ductile Damage Material Model Parameters for a High Strength Steel, Nordic Steel Construction Conference: 23/09/2015–25/09/2015, 2015 231–232 http://urn.kb.se/resolve?urn=urn:nbn:se:ltu:diva-37833.
[28] M. Feldmann, N. Schillo, S. Schaffrath, K. Virdi, T. Björk, N. Tuominen, M. Veljkovic, M. Pavlovic, P. Manoleas, M. Heinisuo, K. Mela, Rules on High Strength Steel, https://op.europa.eu/en/publication-detail/-/publication/515285b0-c820-11e6-a6db-01aa75ed71a1/language-en/format-PDF/source-194823584 2016.
[29] R. Yan, H. Xin, M. Veljkovic, Identification of GTN Damage Parameters as a Surrogate Model for S355, 2020 582–589, https://doi.org/10.3850/978-981-11-0745-0_066-cd.
[30] J. Fish, Practical Multiscaling, 2013.
[31] ABAQUS, Abaqus Analysis User's Manual, 2019 Version, 2019.
[32] C.C. Roth, D. Mohr, Ductile fracture experiments with locally proportional loading histories, Int. J. Plast. (2016) https://doi.org/10.1016/j.ijplas.2015.08.004.
[33] H.W. Swift, Plastic instability under plane stress, J. Mech. Phys. Solids. 1 (1952) 1–18, https://doi.org/10.1016/0022-5096(52)90002-1.
[34] E. Voce, The relationship between stress and strain for homogeneous deformation, J. Inst. Met. 74 (1948) 537–562.
[35] ISO S. 6892–1: 2010, Metallic Materials. Tensile Testing. Part 1: Method of Test at Room Temperature, 2010.
[36] L.-J. Jia, H. Kuwamura, Ductile fracture simulation of structural steels under monotonic tension, J. Struct. Eng. 140 (2014), 04013115 https://doi.org/10.1061/(asce)st.1943-541x.0000944.
[37] Y.Z. Wang, G.Q. Li, Y.B. Wang, Y.F. Lyu, H. Li, Ductile fracture of high strength steel under multi-axial loading, Eng. Struct. 210 (2020) 110401, https://doi.org/10.1016/j.engstruct.2020.110401.
[38] R. Yan, H. El Bamby, H. Xin, M. Veljković, Fracture Simulation of Welded HSS Hollow Section X-JOINT, 2022.
[39] Y.B. Wang, Y.F. Lyu, Y.Z. Wang, G.Q. Li, J.Y. Richard Liew, A reexamination of high strength steel yield criterion, Constr. Build. Mater. 230 (2020) 116945, https://doi.org/10.1016/j.conbuildmat.2019.116945.
[40] Y. Huang, B. Young, The art of coupon tests, J. Constr. Steel Res. 96 (2014) 159–175, https://doi.org/10.1016/j.jcsr.2014.01.010.